Electric Field of the CERES TPC

D. Miśkowiec

October 5, 2007

Contents

1 Historical introduction

In May 1998 first laser tracks were measured with the TPC. The tracks showed a curvature in drift time vs. z dubbed "smile" (Fig. 1). The electric field map used at that point was the one coming from a two-dimensional calculation (r, ϕ) assuming uniformity in z. Subsequently, ShinIchi performed a 3-d calculation using Mafia and Maxwell [1]. The curvature decreased somewhat but did not disappear entirely. ShinIchi tried varying various parameters and found some configurations which would straighten the tracks but which, at the same time, would require unreasonably large geometrical or electrical distortions to be considered realistic.

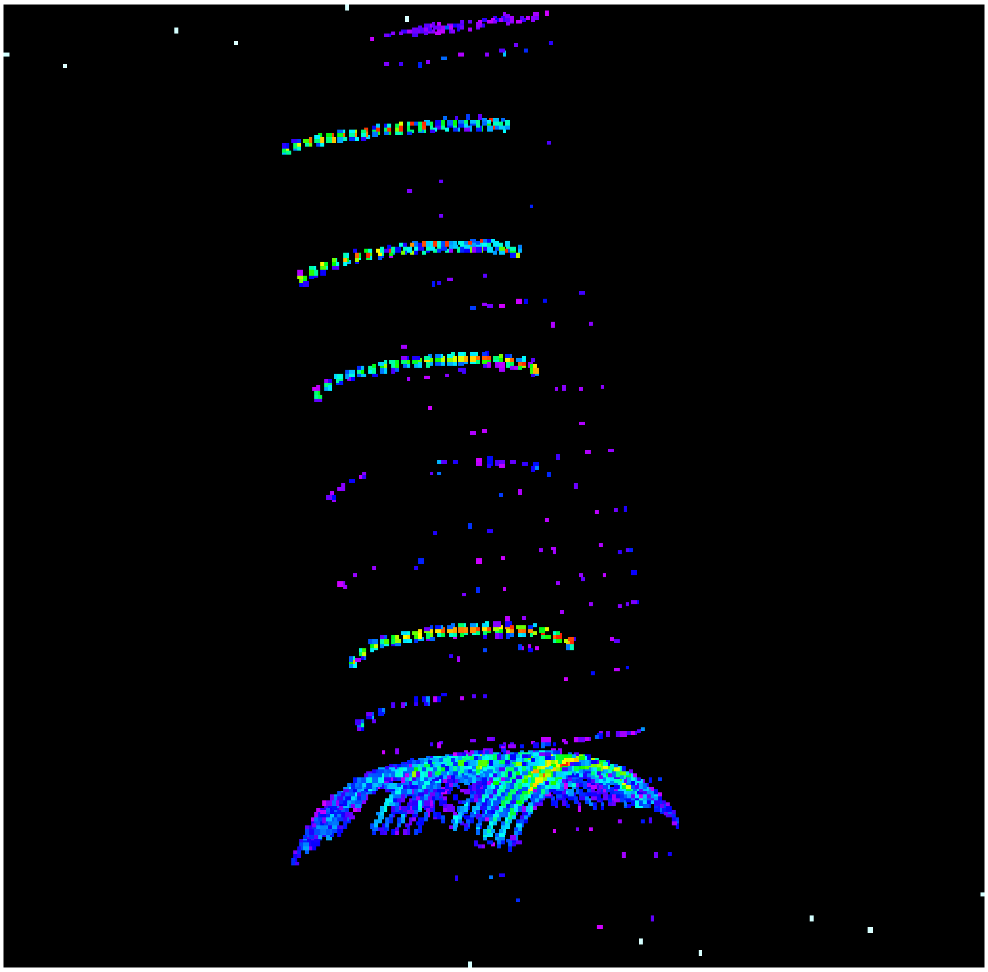

Figure 1: Reconstructed laser tracks, showing curvature in r vs. z (negative smile). The many hits at the bottom come from electrons knocked out of the high voltage cylinder by stray laser light.

In the analysis of the 99 data Ana phenomenologically adjusted the radial component of the electric field in a z-dependent way such to make the particle tracks, measured without magnetic field, straight.

In 1999-2001 Pavel Akishin, mathematician from Dubna, calculated the electric field by a custom finite-element based method. Subsequently, he varied ring potentials in steps of 10% to find the field which produces straight laser tracks. Rather than recalculating the field for each set of potentials, he calculated a set of elementary fields defined by setting one ring to 1 V and all other elements to ground. Since the Poisson equation is linear in the potential, any linear combination of these elementary fields can be added to the nominal field. When optimizing the ring potentials it is then enough to vary the coefficient of this linear combination and redo drift. I learned this powerful method from him and used it to optimize the correction fields (Section 7).

I started my calculation of the TPC electric field in 2001 in the hope that a careful implementation of geometry and boundary conditions would straighten the smile - but it did not. The field obtained was similar to ShinIchi's one, not sensitive to adding more and more geometrical details, and not accounting for the smile. Then I started looking for effects which could affect the voltage of the field cage rings and thus distort the field at the ends of the TPC. As one of the first things I calculated the TPC field in absence of the endcup field cages. The distortion in this case was much larger than the observed one. Subsequently, the following phenomena were considered:

continuous current from rings to ground

: Ions contained in the CO_2 gas, which fills the 80 (82) mm gap between the field cage foil and the upstream ground foil (downstream aluminum backplate), serve as charge carriers. The smile then should be different upstream and downstream, and should depend on beam intensity. The smile could be accounted for if every ring was connected to ground via a 60 GOhm resistor. For this, the gas resistivity would have to be as low $4{\cdot}10^{12}$ Ohm cm. This has been excluded.

discharges from rings to ground

: The dielectric strength of CO_2 was estimated to be 1.2-2.6 kV/mm. This is more than 30 kV/80 mm = 0.38 kV/mm, the highest field in the CO_2 volume.

current between adjacent rings

: Excluded: CO_2, $NeCO_2$ kapton, and quartz glass (laser windows) resistivities are high enough.

discharges between adjacent rings via gas

: The dielectric strength of $NeCO_2$ and CO_2 were estimated to be 0.5-1.2 kV/mm and 1.2-2.6 kV/mm, respectively. Both are higher than 1.4 kV/5.46 mm = 0.26 kV/mm, the highest field between two adjacent rings.

charging of the field cage kapton

: This effect is mentioned in the Blum-Rolandi bible. Other experiments protect against it by using double layers of interleaved strips (ALEPH, HARP) or by suspending the strips in the air (well, gas) rather than on kapton (NAA49, ALICE). It is not excluded and it would mean beam intensity dependence.

variation of the voltage divider resistance with temperature

Carbon resistors vary their resistivity with the rate of $8{\cdot}10^{-4}$ K^{-1}, other types four times less [2]. With reasonable temperatures assumed this is not enough to account for the smile.

short between two adjacent rings

A Maxwell calculation demonstrated that the distortion introduced by this does not reach the drift region which starts 10 cm from the field cage foil.

disconnected (floating) ring

A Maxwell calculation with a conductor placed between the capacitor plates demonstrates that a floating conductor acquires a voltage which is between the voltages of its neighbors. The distortion introduced by a floating ring would not reach the drift region. Furthermore, the 2001 measurements of the downstream field cage strip potentials with reduced voltage showed no floating ring.

ring on ground

A ring on ground could account for the observed smile. It is, however, not clear how a ring could acquire and maintain the ground potential. Furthermore, the 2001 measurements of the downstream field cage strip potentials with reduced voltage showed no ring on ground.

A break-through happened when Chilo revisited his old plot of current vs. voltage and discovered that the voltage-to-current ration was voltage dependent. The origin of this has been tracked down to the carbon resistors changing their resistance under applied voltage. The effect was approximately R=R0(1-0.3 U) with U being in kV. A calculation with the resistances modified according to this formula, finalized in early 2002, nearly straightened the laser tracks.

In the rest of this note the calculation of the field is described in a logical rather than chronological order. All data and calculations are for magnetic field switched off, B=0.

2 Geometry

The geometry relevant to the electric field calculation is presented in Fig. 2 and the numbers are collected in Table 1. All wire planes were modelled as rectangles of conducting material, kept on a fixed potential. The coordinate system is defined as follows: z follows the beam, x points to Jura, y points up. The units are mm. The origin is on the cylinder axis in the middle of the TPC, i.e. the active part of the readout chambers extends from z=-1000 to 1000 mm. The readout chamber 0 covers $0 < \phi < 22.5$ degrees.

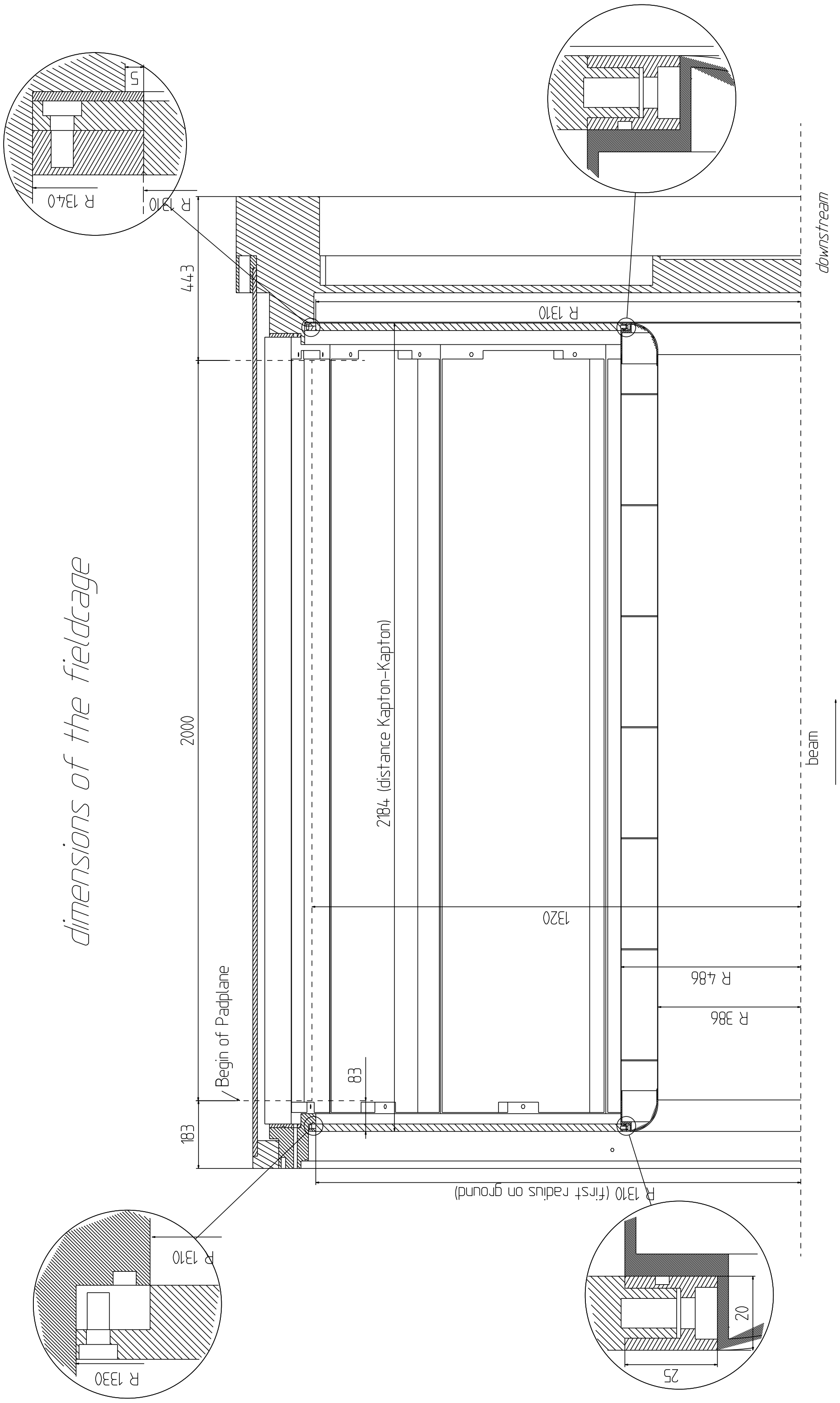

Figure 2: TPC geometry relevant for the electric field calculation [3].

Table 1: Geometry and potentials used in the electric field calculation.

ground cylinder radius	386 mm
high voltage cylinder radius	486 mm
distance between beam axis and gating grid	1308 mm
distance between beam axis and cathode plane nominal	1314 mm
distance between beam axis and cathode plane effective	1312 mm
number of field cage rings	40
field cage ring width in r	15 mm
space between two field cage rings in r	5.46 mm
ring 1 min radius	491.46 mm
ring 1 max radius	506.46 mm
ring 2 min radius	511.92 mm
ring 2 max radius	526.92 mm
ring 40 min radius	1289.40 mm
ring 40 max radius	1304.40 mm
ground ring upstream min radius	1310 mm
azimuthal angle range covered by one chamber	22.5 degree
gating grid wire length	490 mm
gating grid plane length in z	2000 mm
gating grid plane center in z (by definition)	0 mm
upstream ground foil position in z	-1163 mm
upstream fieldcage position in z	-1083 mm
downstream fieldcage position in z	1101 mm
downstream backplate position in z	1183 mm
ground cylinder potential	0 V
high voltage cylinder potential	-29200 V
gating grid potential when open	-140 V
cathode plane potential	0 V
field cage ring potentials	see next section

The geometry and the potentials of a readout chamber (azimuthally in the middle) are shown in Fig. 3. The drifting electrons arrive from the left. At x (transverse distance from the beam axis) of 1308 mm they pass through the gating grid, the wires of which are kept on -140 V. Subsequently, they traverse the cathode plane (ground potential) and arrive to the anode wires (+1400 V). In the calculation, the three-dimensional electron drift stops at the gating grid. After that a single 6 mm step is performed from the gating grid to the cathode plane.

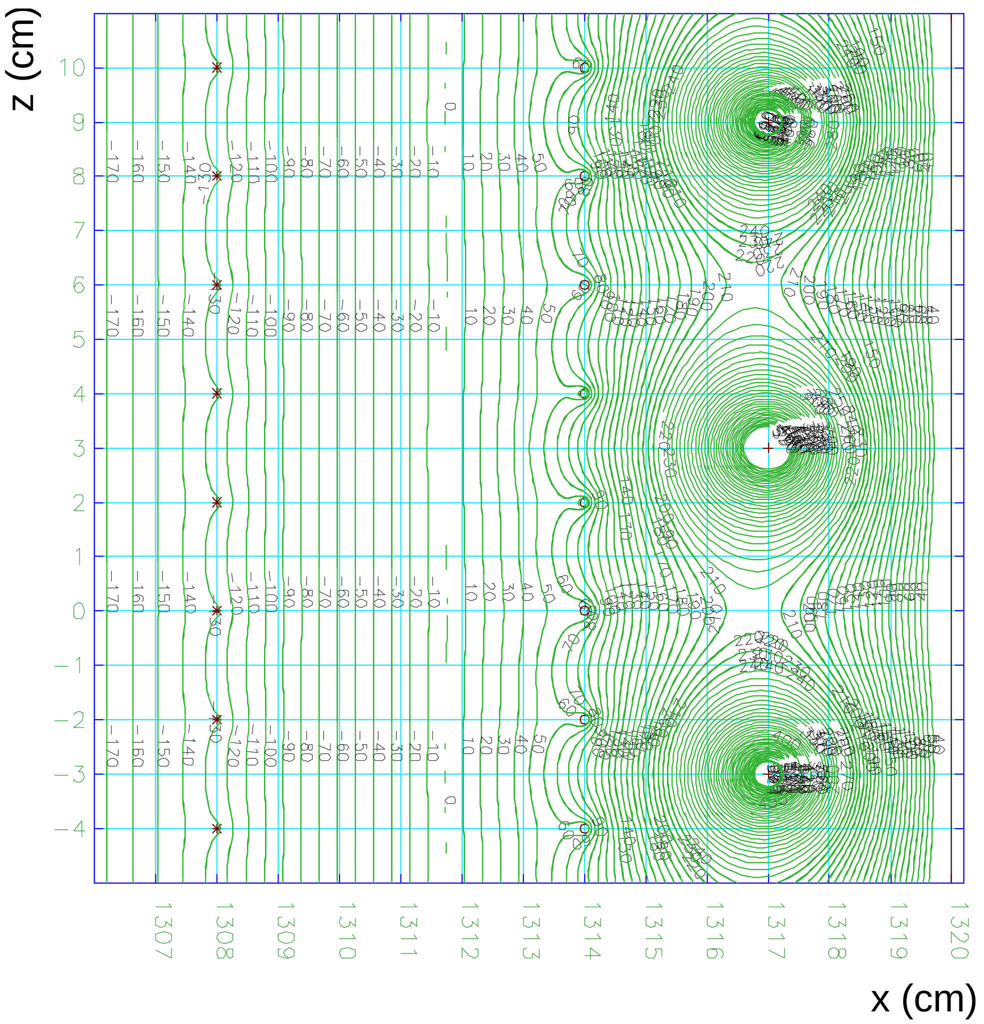

Figure 3: Garfield calculation of the readout chambers. Shown are equipotential lines. The gating grid wires at x=1308 mm and the cathode plane wires at x=1314 mm are kept at -140 and 0 V, respectively. However, because of the leakage of the field, the effective -140 and 0 V planes are at x=1307.5 mm and 1311.7 mm, respectively.

A gating grid potential of -140 V would match exactly a drift field defined by the -30 kV cylinder potential on one side and the grounded cathode plane at x=1314 mm on the other. However, the leakage of the anode field through the cathode plane, effectively shifting the ground plane from x=1314 mm to about 1312 mm, and the fact that the actual cylinder potential is -29.2 kV lead to a certain mismatch, visible at the gating grid plane x=1308 mm. The distortion is even larger closer to the edge of the chamber, where the distance from the cylinder is larger (Fig. 4). The resulting average (averaged over z across the grid wire distance) potential at the gating grid plane r=1308 mm acquires values between -110 and -126 V, depending on z and ϕ. The potential map $V_{gg}(z, \phi)$ is used as the boundary condition when calculating the three-dimensional electric potential map (Section 6).

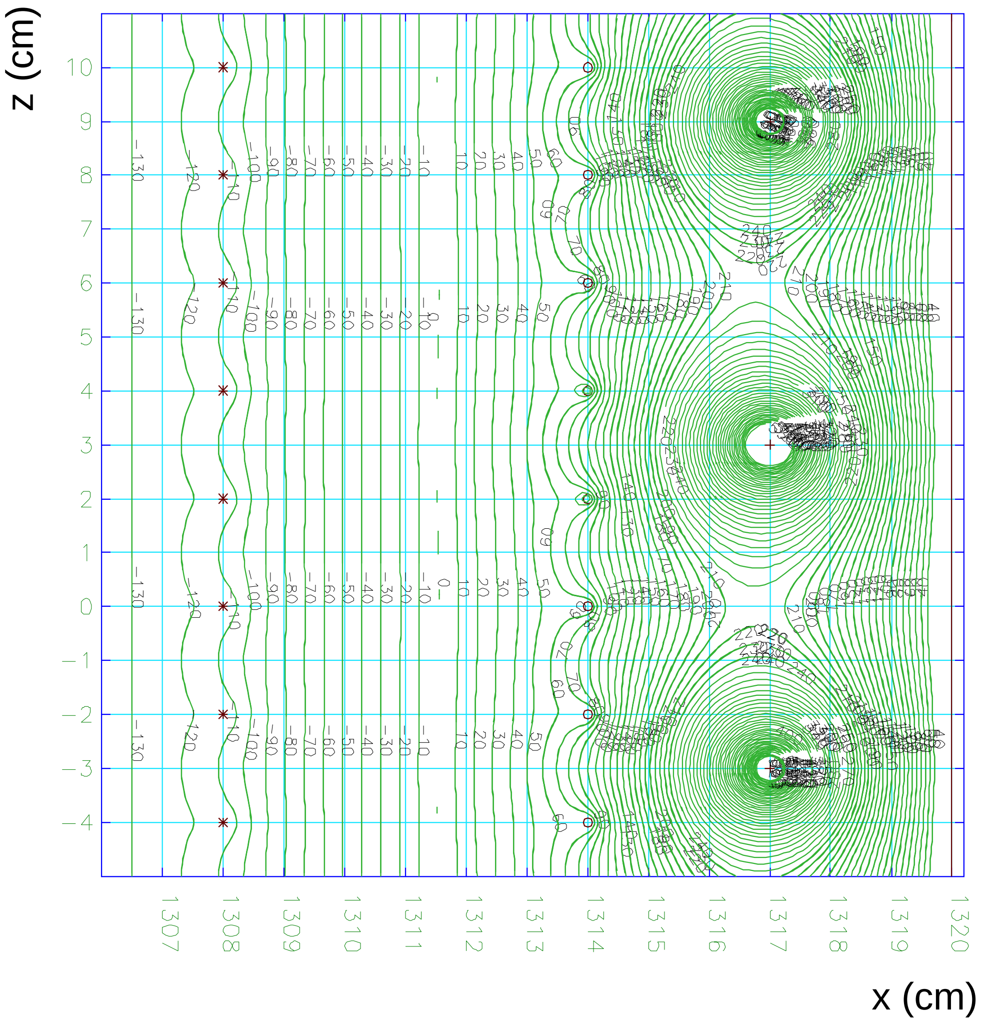

Figure 4: Same as Fig. 3 but at the edge of the chamber, ϕ=11°.

The z-coordinates of the 20 readout planes are assumed to be -957, -855, -753, -651, -567, -465, -363, -261, -177, -75, 27, 129, 261, 363, 465, 567, 651, 753, 855, and 957 mm. The y-coordinates of pads in mm, in respect to the azimuthal center of a chamber, are obtained by the following FORTRAN formula:

```
y=(pad-23.5)*10.3
if (pad.lt.0.5) y=y+1.1
if (pad.gt.46.5) y=y-1.1
```

3 Field cage ring voltages

The TPC field cage high voltage scheme is shown in Fig. 5. A negative high voltage of 29.2 kV (see Section 4) is applied to the cylinder via a 0.5 MOhm resistor. Two resistor chains, connected to the cylinder on one side and to the ground on the other, supply potentials to the upstream and downstream rings. The two currents are measured via the voltage drop on the external 9.95 kOhm test resistors in series with the chains.

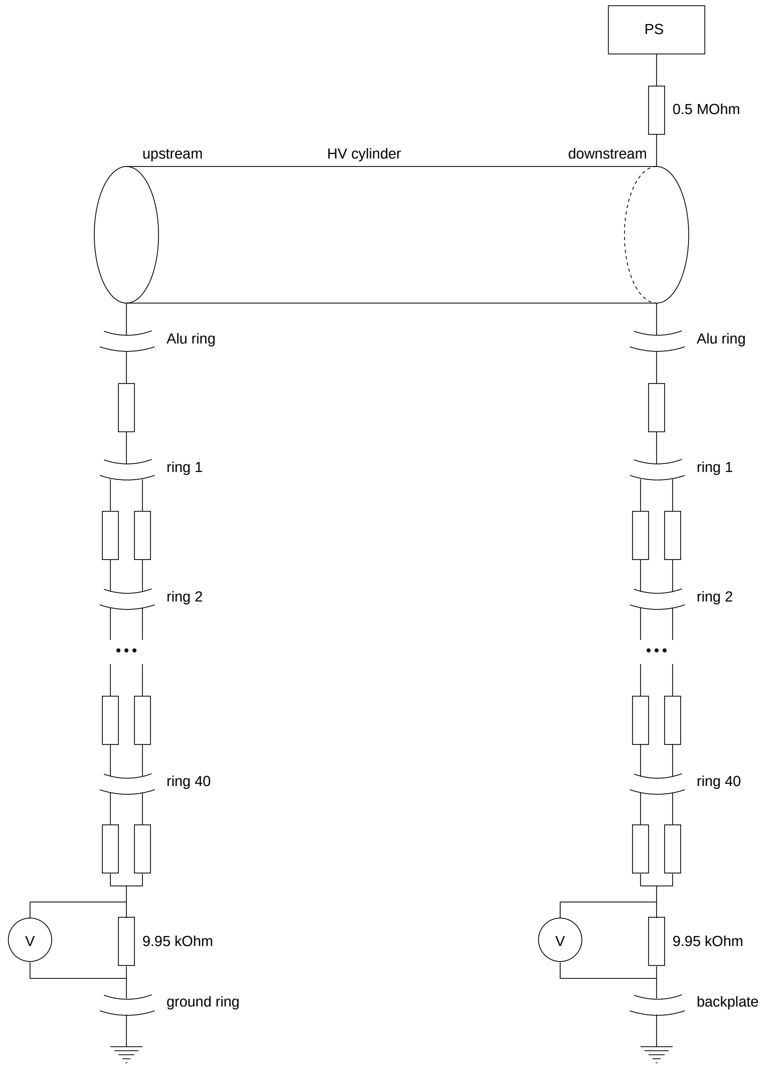

Figure 5: Voltage scheme of the field cage. A high voltage of about -30 kV is applied to the cylinder. Two resistor chains supply potentials to the upstream and downstream rings. The two field cage currents are measured via the voltage drop on the 9.95 kOhm test resistors.

A reanalysis of the 1998 voltage-current data demonstrated that the resistance of the field cage voltage divider was changing with the applied voltage (left panel of Fig. 6). Moreover, in 1999 a short between two rings appeared in the downstream chain. The short develops at around 20 kV when ramping the voltage up (right panel of Fig. 6), and stays there around normal running voltage which is about 30 kV.

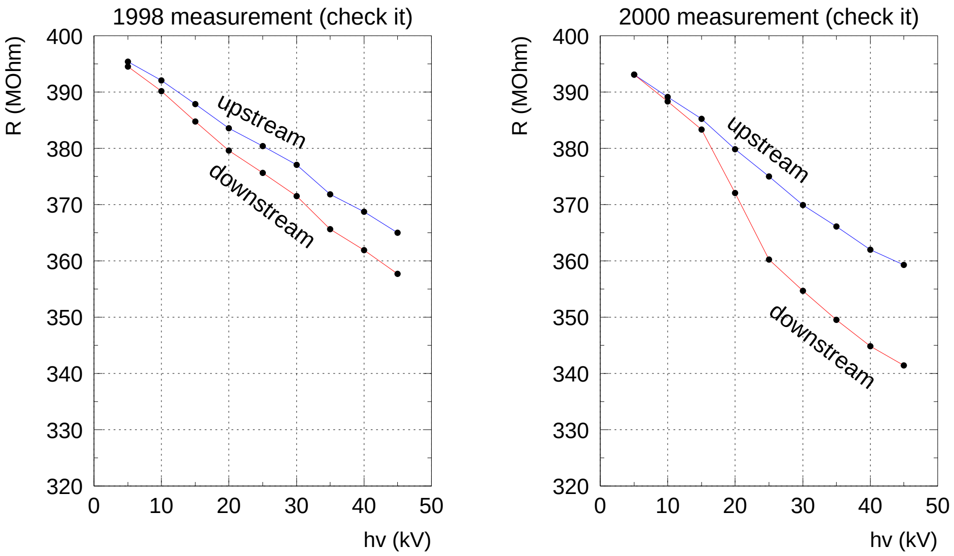

Figure 6: Resistance of the field cage voltage dividers. The slope is caused by resistors which change their resistance under load. The additional jump in the downstream chain in 2000 (red line in the right hand plot) is caused by a short between two rings which develops at about 20 kV. The systematic error of the absolute scale is 5%.

The field cage voltage dividers contain two kinds of resistors: metal and carbon ones. A laboratory test, performed after the discovery of changing divider resistance, demonstrated that while the metal resistors were stable, the carbon resistors were linearly decreasing their R with the applied voltage:

$$R = R_0(1 - b\,U), \tag{1}$$

with the badness $b = 0.1 - 0.3$ kV^{-1}.

In May and July 2001 two calibration measurements were performed in which the CO_2 volume was opened such that one could reach to the field cage rings and measure their voltages. The measurements showed a good agreement with the resistor map [2] and suggested a badness of 0.26-0.28 kV^{-1}. The short was localized to be between the aluminum ring and ring 1.

In order to calculate the ring potentials for a given cylinder voltage and a given badness (assumed to be same for all carbon resistors) we proceed as follows. We first assume the nominal resistance of the chain resistors. With this we calculate the voltages between the rings. Using the resistor map we calculate the voltage applied to each single resistor. Then we modify the resistance of the carbon resistors accordingly. With the new resistances we recalculate the voltages. The result becomes stable after 2-3 iterations.

4 Cylinder potential

During the 2000 run the TPC cylinder was kept at a voltage at which the needle of the power supply was showing -30 kV. More precisely, the voltage was adjusted such that the voltage drop on the test resistors of 9.95 kOhm was 0.788 V and 0.830 V for the upstream and downstream chains, respectively, the difference attributed to the downstream short. The measured voltage drop values constrain the possible badness/cylinder voltage values to the inclined lines shown in Fig. 7. Calibration of the power supply in September 2001 constrains the absolute value of the cylinder voltage in 2000 to 29.2-29.6 or to 28.7-29.5 kV, depending on the data analysis method. The value of badness needed to straighten the smile of laser rays is represented by the hor-

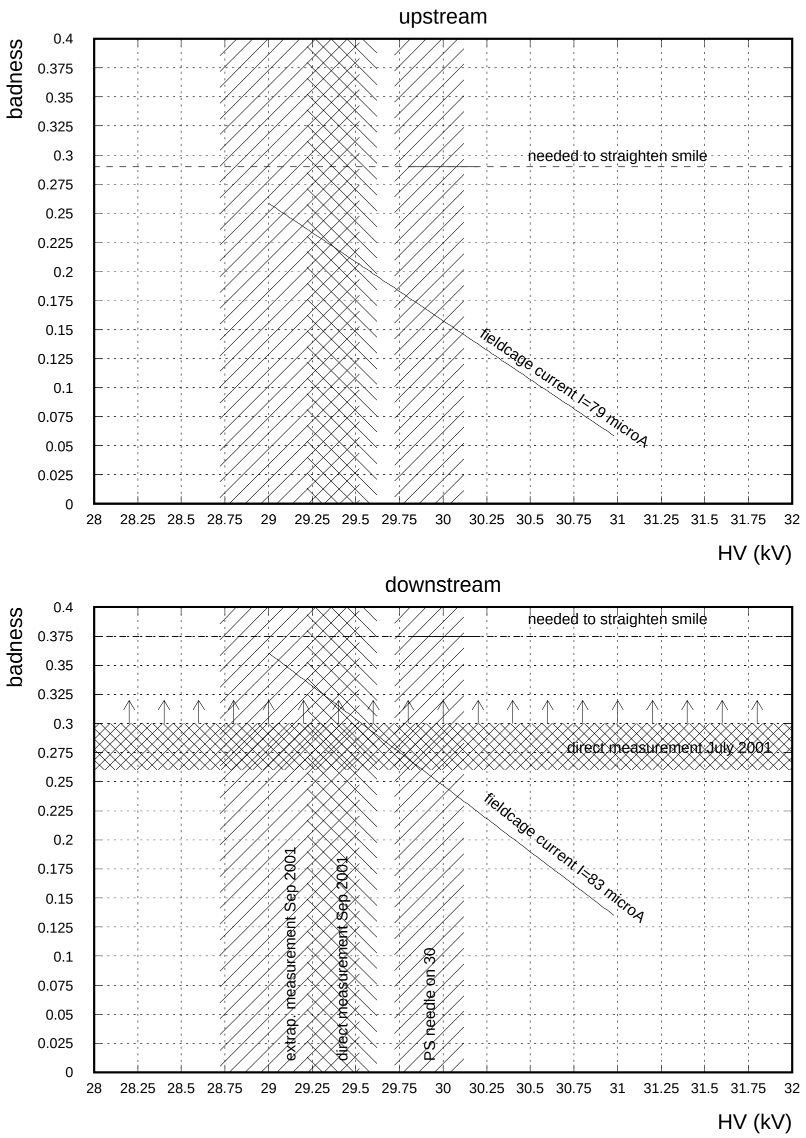

Figure 7: Compilation of data concerning the resistor badness and the cylinder voltage.

izontal dashed line. The horizontal shaded area in the lower plot shows the result of the direct measurement of ring voltages downstream, with vertical arrows representing a correction accounting for the behavior of the power supply used. The badness in the upstream chain seems to be lower than in the downstream, indicated both by the current measurements (inclined line) and the laser tracks (dashed horizontal). We attribute this fact to possible deviations from the resistor map in the upstream chain. Based on the figure and on the fact that laser data taken with magnetic field seemed to prefer lower drift fields we assumed the cylinder potential to be -29.2 kV and used a badness of b=0.24 and 0.34 kV^{-1} for upstream and downstream, respectively.

5 Three-dimensional field calculation with Maxwell

Since I thought a precise implementation of geometry and the boundary conditions was the key to explaining the smile I first decided to use Maxwell [4] which has good abilities of representing complex geometries. I started implementing the whole TPC at once but the calculation time quickly started to be an issue and thus I had reduce the setup to 1/4 of the TPC, then to 1/16 (one chamber), then to 1/2 of a chamber, and finally to two separate calculations of a 1/4 chamber each (there is no upstream-downstream symmetry but one can safely assume that E_z=0 at z=0). A screen shot of a 1/2-of-a-chamber calculation (geometry + equipotential lines) is shown in Fig. 8. Reducing the size of the modelled object and exploiting the symmetry allowed to increase the

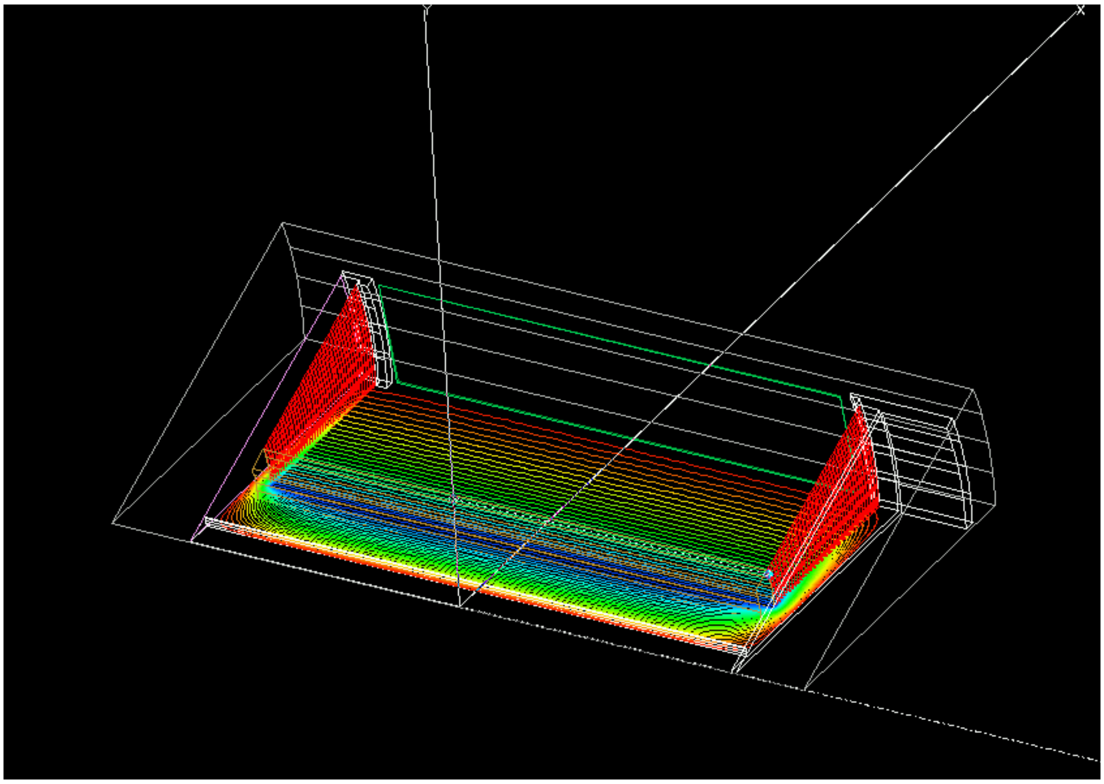

Figure 8: Equipotential lines calculated with Maxwell for an azimuthal slice of 1/32 of the TPC corresponding to half a read-out chamber.

precision of the calculation while keeping a reasonable execution time. However, even in a 6 CPU-days calculation of an 1/4 chamber the numerical precision turned out not sufficient (see Fig. 9).

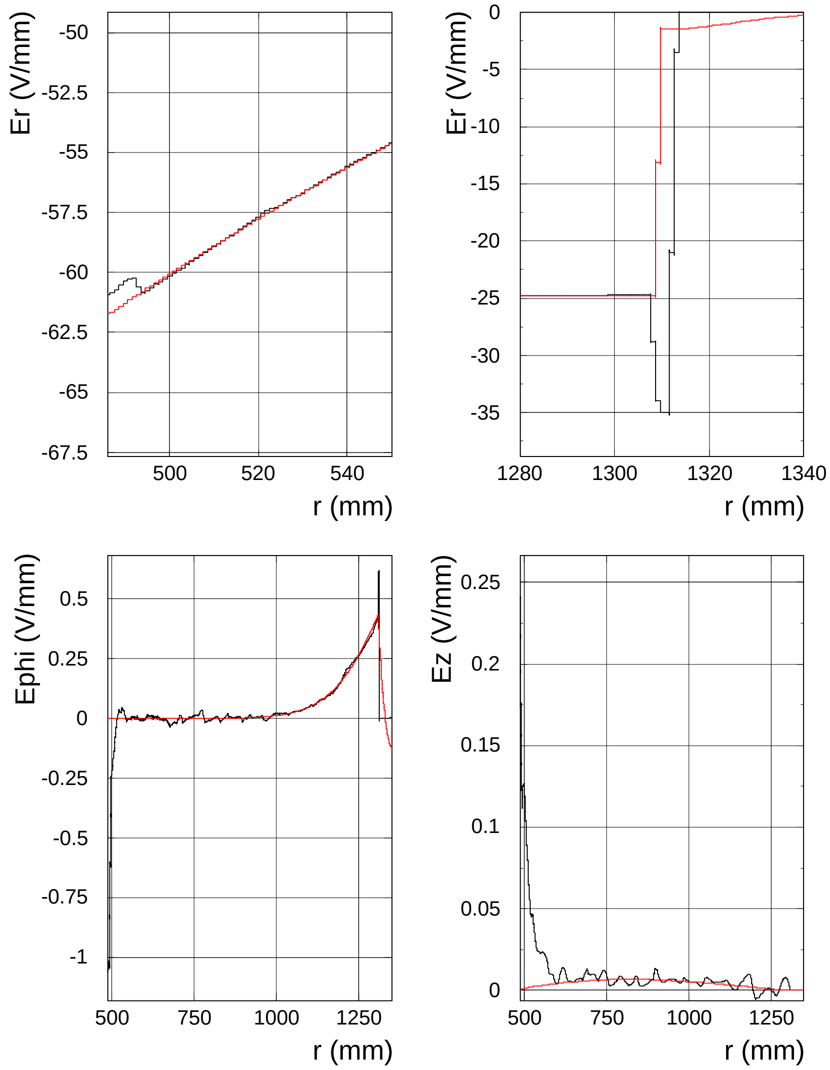

Figure 9: Electric field calculated with Maxwell (black line). Finite numerical precision is visible. The red line represents custom calculation with mymax (Section 6).

6 Three-dimensional field calculation with mymax

We decided to smooth out the bumps in the potential calculated with Maxwell. Linear smoothing would be not appropriate because the potential is a non-linear function of the coordinates. Instead, we implemented a smoothing which obeys the Poisson equation. Next we adapted the code such that the boundary conditions were fulfilled.

At this point the smoothing code reached such a degree of maturity that it did not need Maxwell field anymore. It would start from any potential and ultimately smooth it to the proper solution. We called the code mymax. One mymax run gives a potential of half-a-chamber, i.e. 1/32 of the TPC. Being tailored to our geometry it is orders of magnitude faster than Maxwell and it produces no significant bumps, see Fig. 9. For reasons of speed mymax first calculates field on a rough grid (grid5, see Section 10) and then on a finer one (grid3). An example of the calculated potential is shown in Fig. 10.

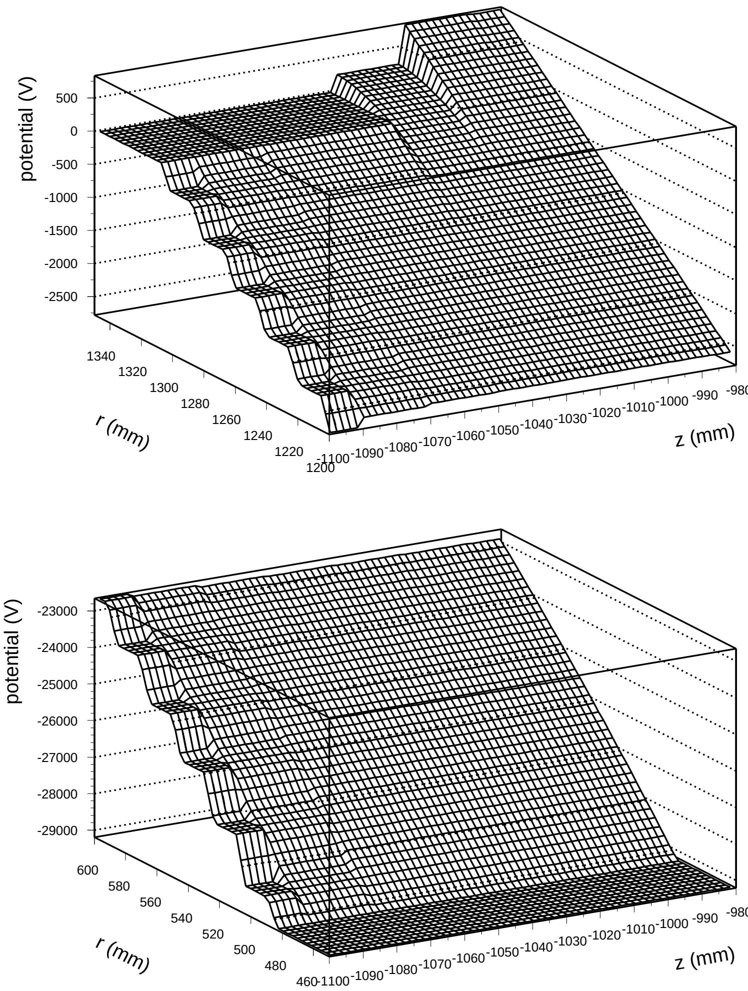

Figure 10: Three-dimensional electric potential $V(r,z)$ (ceres087.grid3) calculated with mymax for one half of a chamber in the vicinity of the upstream end of the TPC. The steps are caused by the field cage rings. The calculation grid is (dr,dϕ,dz)=(1 mm, 0.25$^{\mathrm{o}}$, 2 cm).

7 Residual smile correction fields

Laser tracks, reconstructed under an assumption of an electric field uniform in z, would deviate from a straight line up to $\Delta r \approx 4$ cm at the ends of the TPC (track at r=600 mm). The three dimensional calculation with nominal geometry and voltages brought the curvature down to about 2.5 cm. Accounting for the actual resistance of the ring voltage divider chains, as described in Section 3, further reduced the deviation to $\Delta r \approx 6$ mm . The rest was fixed by applying a phenomenological correction, consisting in adding a linear combination of three elementary potential maps calculated

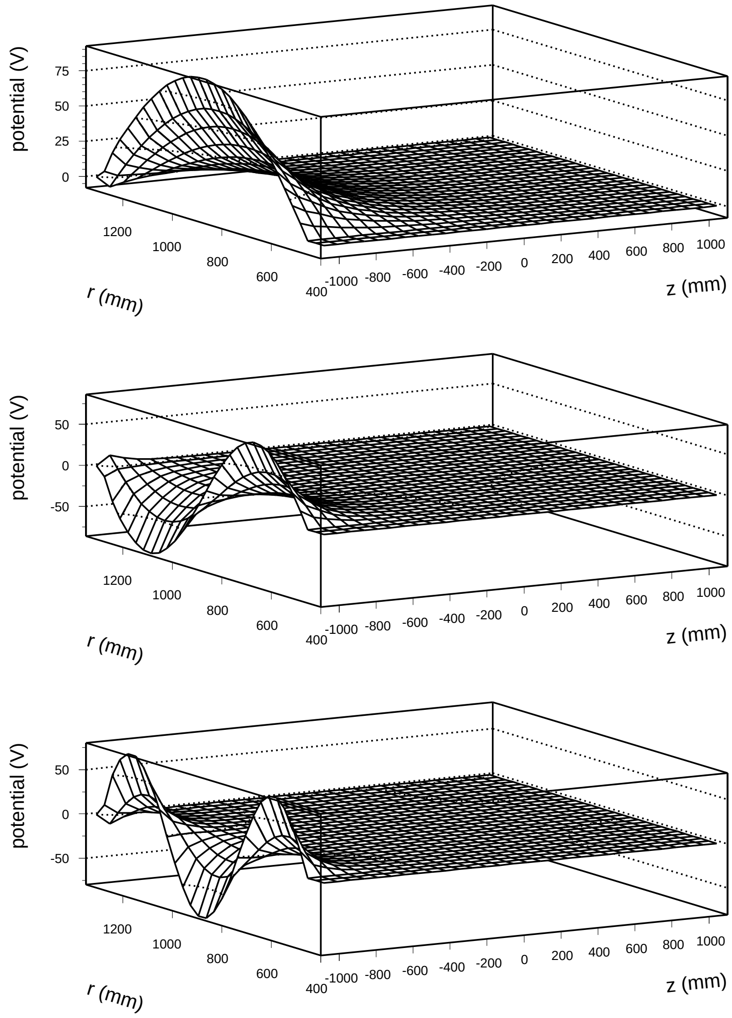

Figure 11: The elementary correction potential maps (from top ceres180.grid3, ceres181.grid3, ceres182.grid3) for the upstream end of the TPC.

with mymax using the following voltages of the divider rings:

$$U_1(r) = 100\text{ V} \cdot \sin\left(\pi \frac{r-486}{1310-486}\right) \quad (2)$$

$$U_2(r) = 100\text{ V} \cdot \sin\left(2\pi \frac{r-486}{1310-486}\right) \quad (3)$$

$$U_3(r) = 100\text{ V} \cdot \sin\left(3\pi \frac{r-486}{1310-486}\right) \quad (4)$$

with r being in mm, and r=486 mm and 1310 mm being the radii of the HV cylinder and the ground cylinder, respectively (Fig. 11).

The three coefficients were optimized independently for the upstream and the downstream end of the TPC, with the straightness of the laser tracks being the criterium. The resulting correction potential map is shown in Fig. 12.

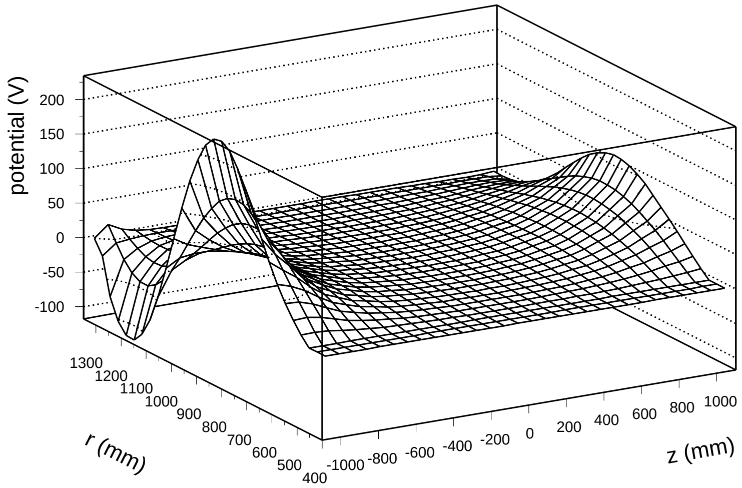

Figure 12: The residual smile correction potential map (ceres091.grid3). The correction is larger at the upstream end of the TPC.

8 Chamber misalignment correction fields (mymax2d)

The three-dimensional field calculation, needed to account at the same time for the polygonal readout chambers ($r(\phi) \neq$ const) and for the track curvature in $r(z)$, was done for performance reasons only for a 11.25° slice in ϕ of the TPC (half a chamber). The azimuthal symmetry, however, is broken by the misalignment of the 16 chambers. To account for this, a number of two-dimensional potential calculations $V(r, \phi)$ was performed for a complete set of 16 chambers (Fig. 13), and then repeated with one of the chambers being slightly displaced in r or tilted in r vs. ϕ (Fig. 14). The numerical technique of the calculation was similar as the three-dimensional case.

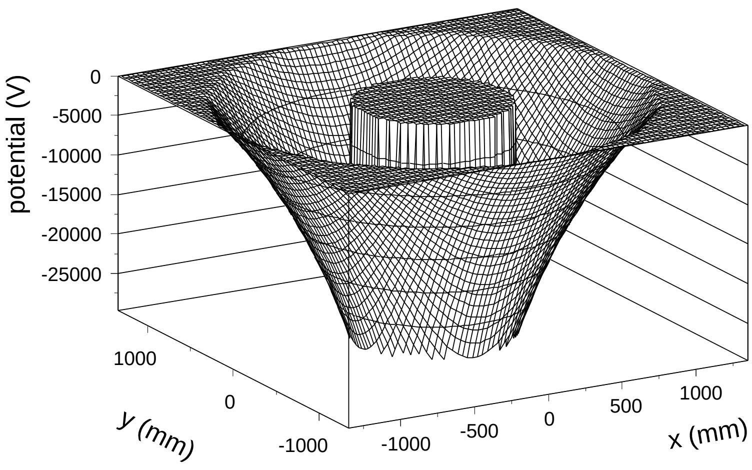

Figure 13: Two-dimensional electric potential $V(r, \phi)$ calculated with mymax2d with all chambers at their nominal positions.

The correction potentials, defined as a difference between a two-dimensional calculation for a displaced (or tilted) and a perfectly aligned chamber

$$V_{cor}(r, \phi) = V_{misaligned}(r, \phi) - V_{ideal}(r, \phi) \tag{5}$$

were then added to the three-dimensional calculations, separately for each chamber and each z-plane. The displacements in r and the tilts in $r(\phi)$ were chosen such to move the position of the high voltage cylinder, visible in the data either via the electrons knocked out from aluminum by the laser light or as the edge in the radial distribution of hits in physics events, as close as possible to the nominal $r = 486$ mm. One should note that displacing a chamber affects the reconstructed cylinder position in two ways: via the

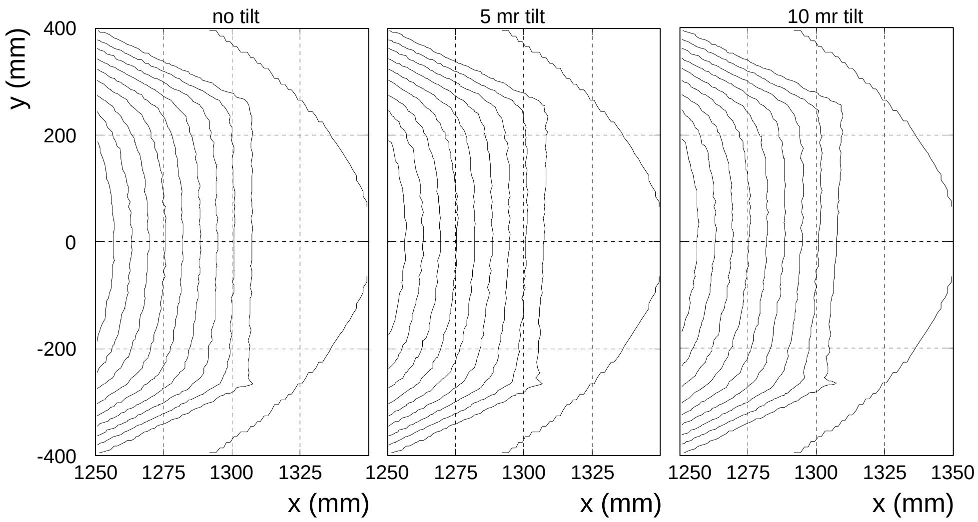

Figure 14: Equipotential lines calculated with mymax2d with the chamber at its nominal position (left) and with two values of tilt (middle and right). Correction maps, defined as the difference between a displaced map and a nominal one, were added to the three-dimensional potential calculated with the ideal geometry.

modified field and via the change in the path length. Both mechanisms were studied separately and in combination. Displacing a chamber by 1 mm without changing the field shifts the reconstructed cylinder by 3 mm (this is because the drift velocity close to the cylinder is three times higher than at the chamber). Using a field calculated with a chamber displaced by 1 mm but keeping the path length unchanged also gives a 3 mm shift. The combination of the two (as expected in a real case) gives a 4-5 mm shift. Figures 15,16 and 17,18 show the HV cylinder position reconstructed before and after applying this correction, respectively. The data in the figures have been corrected for tribump (see next section). Table 2 lists the obtained values of displacements and tilts for each chamber and each plane.

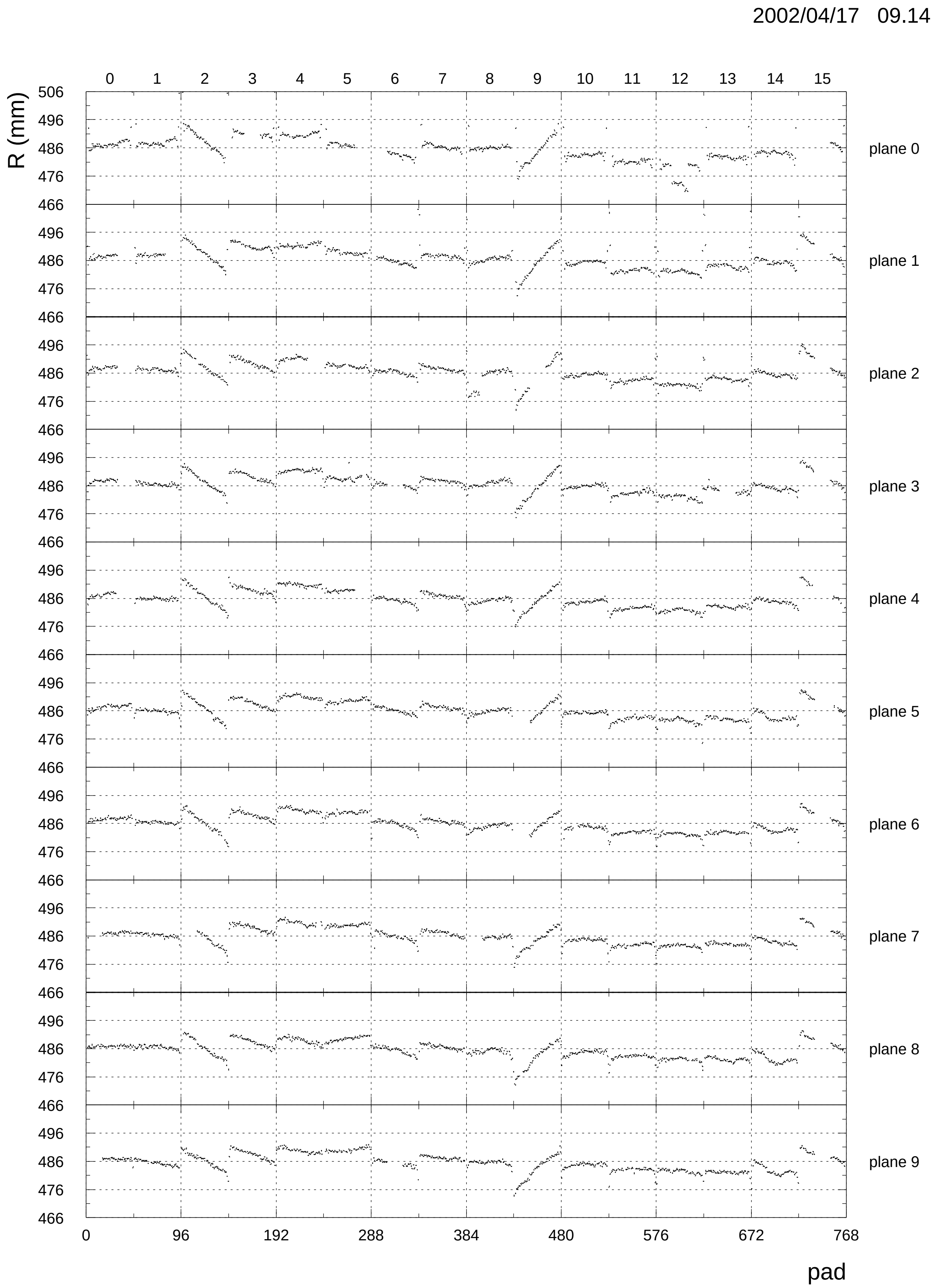

Figure 15: Reconstructed edge of the radial distribution of hits before correcting for chamber positions, planes 0-9.

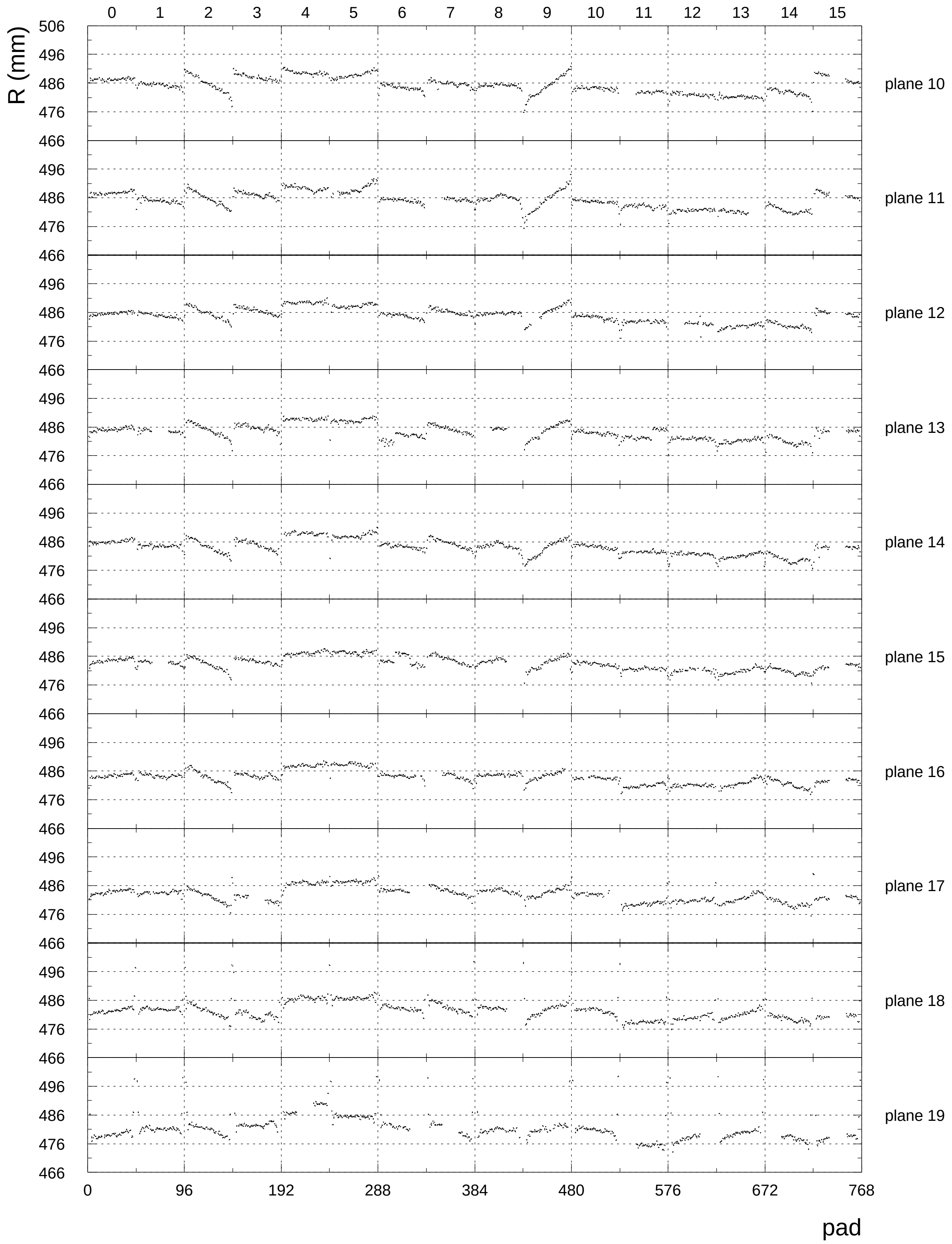

Figure 16: Reconstructed edge of the radial distribution of hits before correcting for chamber positions, planes 10-19.

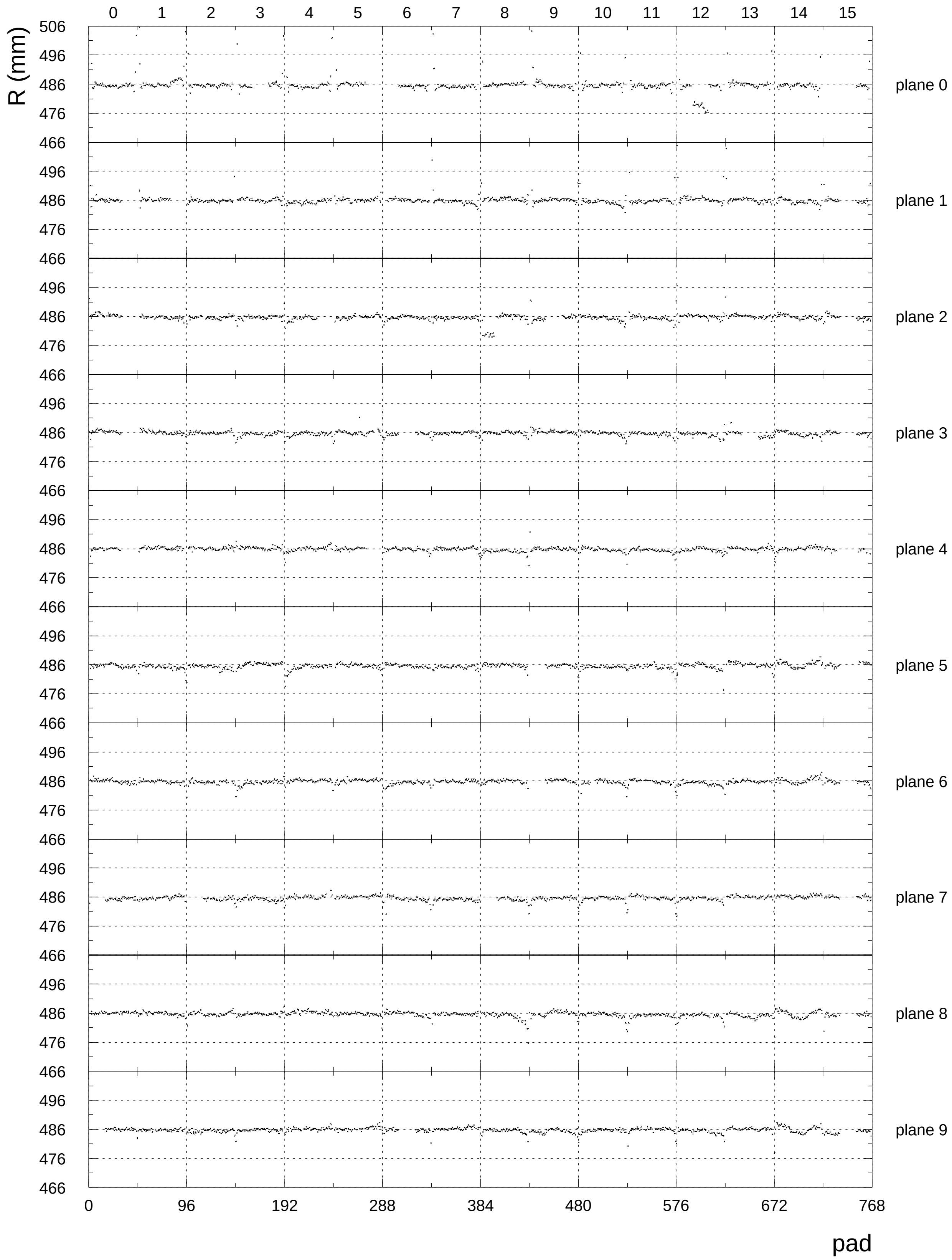

Figure 17: Reconstructed edge of the radial distribution of hits after correcting for chamber positions, planes 0-9.

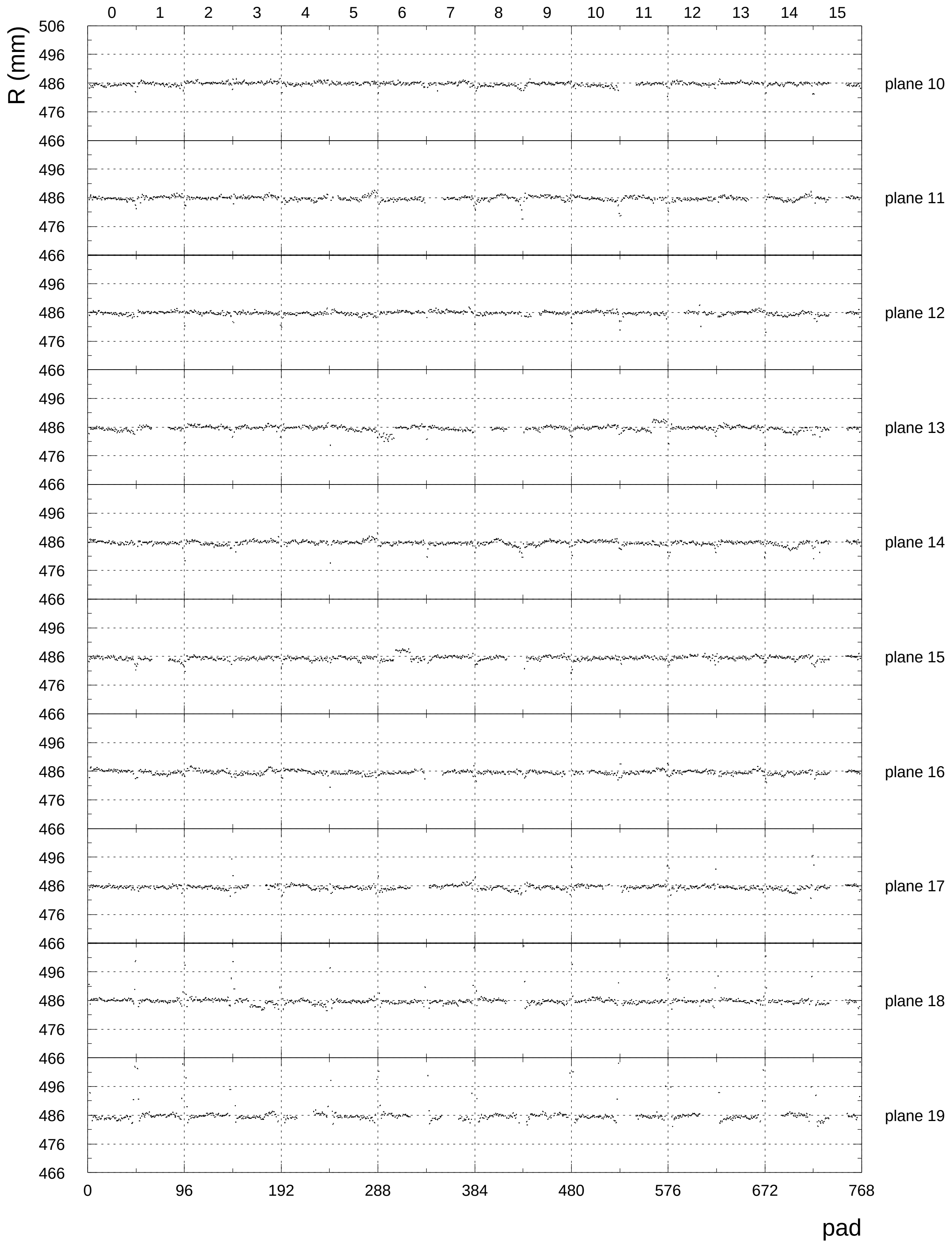

Figure 18: Reconstructed edge of the radial distribution of hits after correcting for chamber positions, planes 10-19.

Table 2: Chamber displacements and tilts needed to bring the reconstructed position of the HV cylinder to its nominal $r = 486$ mm, for each chamber (ϕ) and plane (z). Upper part: the displacement in r in 0.1 mm units. For instance, -13 means the gating grid is at 1308.0 mm - 13*0.1 mm = 1306.7 mm. Bottom part: chamber tilt in mr around the longest axis of a chamber. Positive value means counterclockwise when looking from the downstream end of the TPC.

--	0	1	2	3	4	5	6	7	8	9	10	11	12	13	14	15
0	-4	-4	-6	-8	-10	-2	2	-2	0	2	4	8	10	6	2	-8
1	-4	-4	-6	-10	-10	-6	0	-4	0	2	0	6	8	4	0	-8
2	-4	-4	-6	-8	-12	-6	-2	-4	0	2	0	4	8	4	0	-8
3	-4	-2	-4	-8	-12	-6	-2	-4	-2	2	0	4	6	2	0	-8
4	-4	0	-2	-6	-10	-6	0	-2	0	2	2	6	8	6	2	-6
5	-4	-2	-4	-8	-12	-8	-2	-4	0	2	0	4	6	6	4	-6
6	-4	-2	-2	-8	-10	-8	-2	-2	2	4	2	6	6	6	4	-6
7	-2	-2	-2	-8	-10	-8	-2	-4	0	2	2	6	6	6	4	-6
8	-2	-2	-2	-6	-6	-8	0	-2	0	6	2	4	6	6	6	-6
9	-2	0	-2	-6	-8	-8	0	-2	0	4	2	6	6	8	6	-6
10	-4	0	0	-4	-8	-6	2	0	0	2	2	6	8	10	6	-4
11	-4	2	0	-2	-8	-6	0	0	0	2	2	6	8	10	8	-2
12	0	2	0	-2	-8	-6	2	0	0	0	4	6	8	10	8	0
13	0	2	2	0	-6	-6	4	0	0	2	4	6	8	10	8	2
14	0	2	2	2	-6	-4	2	0	2	4	4	6	8	10	10	4
15	2	2	4	2	-4	-4	2	2	2	4	4	8	10	10	10	6
16	4	2	4	2	-4	-6	2	2	2	2	4	10	10	8	8	6
17	4	4	6	4	-2	-4	2	2	2	4	4	12	10	8	10	8
18	6	4	6	6	-2	-4	4	4	4	6	6	14	10	10	12	10
19	8	6	8	4	-4	-2	4	6	6	6	6	16	12	10	12	12
0	-1	0	4	1	0	1	1	1	-1	-6	0	0	0	0	0	3
1	-1	0	4	1	0	1	1	1	-1	-6	0	-1	0	0	0	3
2	-1	0	4	2	0	1	1	1	-1	-6	-1	-1	0	0	0	3
3	-1	0	4	2	0	0	1	1	-1	-6	-1	-1	0	0	0	3
4	-1	0	4	1	1	0	1	1	-1	-5	-1	-1	0	0	1	3
5	-1	0	4	2	1	-1	1	1	-1	-5	0	-1	0	0	1	3
6	-1	0	4	1	1	0	1	1	-1	-5	0	-1	0	0	1	2
7	-1	1	4	1	1	0	1	1	-1	-4	0	-1	0	0	1	2
8	0	0	4	2	1	-1	1	1	-1	-5	-1	0	0	0	1	2
9	0	1	3	2	1	0	1	1	0	-5	0	0	0	0	1	2
10	0	0	3	1	1	-1	1	1	0	-4	0	0	0	0	1	1
11	-1	1	3	1	1	-1	1	1	0	-5	0	0	0	0	1	1
12	-1	1	2	1	0	-1	1	1	0	-3	1	0	0	0	1	1
13	-1	0	2	1	0	0	1	1	0	-3	1	0	0	-1	1	0
14	-1	0	3	1	0	0	1	2	0	-3	1	0	0	-1	1	0
15	-1	0	2	1	-1	0	1	2	0	-2	1	0	0	-1	1	0
16	-1	0	3	1	-1	0	1	2	0	-2	0	-1	0	-1	2	0
17	-1	0	2	1	-1	0	1	2	0	-2	0	0	0	-2	1	0
18	-1	0	2	0	-1	0	1	2	0	-2	1	0	-1	-2	1	0
19	-1	0	2	0	-1	0	1	2	0	-2	1	0	-2	-1	1	0

9 Tribump: time offset variation across the chamber in ϕ

The reconstructed position of the high voltage cylinder, flattened by shifting and tilting the chambers as described in the previous section, would still show a periodic oscillation when plotted vs. the pad number modulo 48, i.e. across a chamber (Fig. 19, bottom). The three bumps reflect the three Front End Boards of 16 pads each and originate from the pad-by-pad variation of the length of the trace connecting the pad with the readout electronics $L_{ppl}(pad)$ and on the Front End Boards $L_{feb}(pad)$ (Fig. 19, top). The trace length differences are much to small to have any impact on the signal propagation time; however, they affect the measured drift time via the the capacitance and the signal shape. The deviation can be reproduced by a linear combination of the two

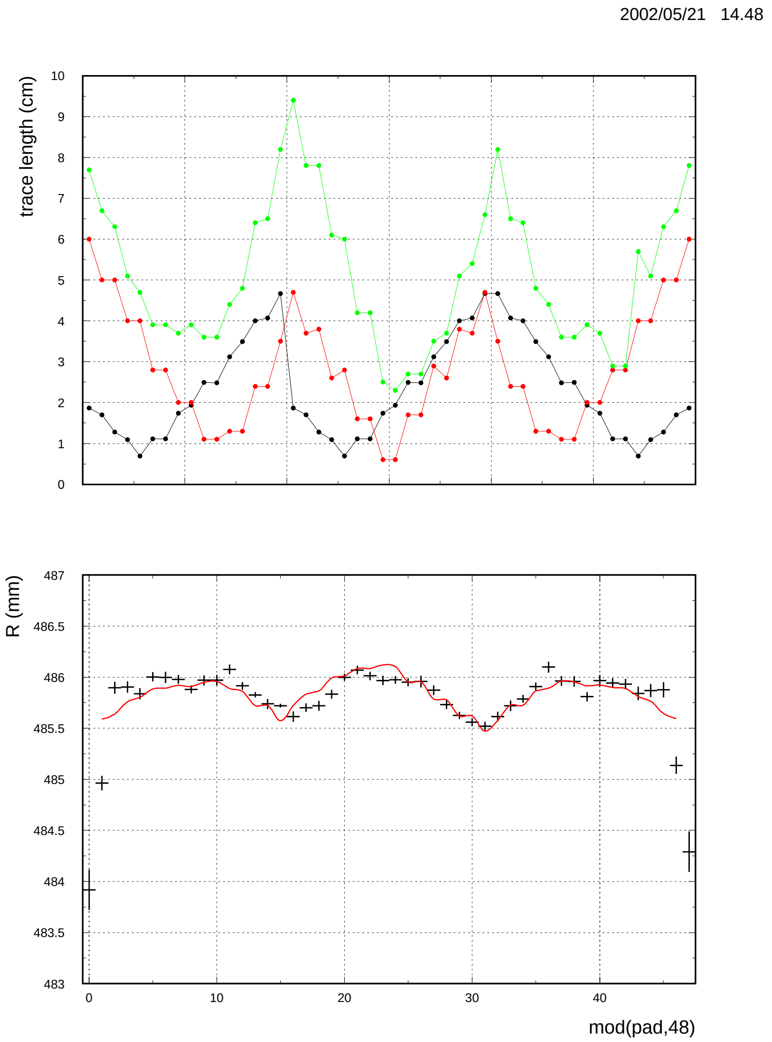

Figure 19: Top: pad trace length on the Front End Board (black) and on the pad plane (red). Green line is the sum. Bottom: periodic oscillation in the reconstructed radius of the high voltage cylinder. The line is a linear combination of the pad plane and FEB trace lengths from the upper plot, with the two coefficients optimized to fit the data.

trace length curves:

$$\Delta r(pad) = 0.10 * L^{'}_{ppl}(pad) + 0.03 * L^{'}_{feb}(pad) \tag{6}$$

for physics events, and

$$\Delta r(pad) = 0.19 * L^{'}_{ppl}(pad) + 0.24 * L^{'}_{feb}(pad) \tag{7}$$

for laser events, with the reconstructed radius correction Δr being in mm and the trace lengths L_{ppl}, L_{feb} in cm. The index *pad* goes from 0 to 47 and measures the azimuthal position within one chamber. The trace length at the azimuthal center of the chamber has been subtracted

$$L^{'}_{ppl}(pad) = L_{ppl}(pad) - \frac{L_{ppl}(23) + L_{ppl}(24)}{2} \tag{8}$$

$$L^{'}_{feb}(pad) = L_{feb}(pad) - \frac{L_{feb}(23) + L_{feb}(24)}{2} \tag{9}$$

and thus the tribumb correction vanishes in the middle of the chamber where the many laser tracks sit and where the electron mobility has been determined.

10 Field data format and location

The results of the Maxwell, mymax, and mymax2d calculations were saved as potential on grid. The grid coordinates are specified in Table 3. The z-index is changing fastest, for example for grid3 the first number is potential at (r,phi,z) = (486,11.25,-1100), the second at (486,11.25,-1080), etc. Only potential values, not the grid, are saved on file.

The potential files are stored locally on `lxial30.gsi.de` in the directory `/work/ceres/field`. Different files correspond to different geometries, boundary conditions, etc. The most important ones are listed in Tables 4 and 5.

The phenomenological smile correction fields 180-192 were calculated as described in Section 6. A linear combination of these fields, chosen such as to minimize the curvature of the laser tracks, was added to the `ceres86` field. The resulting `ceres87` was the final 3-dimensional field map used.

The elementary misalignment correction maps ceres300-330 were calculated as described in Section 8. A linear combination of these fields, chosen such as to bring the reconstructed high voltage cylinder to the nominal r=486 mm, was found for each plane and saved as ceres200-219, and subsequently added to the three-dimensional field.

Table 3: Grids used in electric field calculations; r and z are in mm, ϕ in degrees.

	r-nodes	r-range	ϕ-nodes	ϕ-range	z-nodes	z-range	used for
grid5	109	486-1350	16	11.25-22.5	23	-1100-1100	mymax rough
grid3	865	486-1350	46	11.25-22.5	111	-1100-1100	mymax final
grid6	109	486-1350	480	0-360	1	-1100-1100	mymax2d rough
grid7	865	486-1350	1440	0-360	1	-1100-1100	mymax2d final

Table 4: Three-dimensional potential maps. b=0.24 means ring voltages calculated using the nominal resistor map with the badness of 0.24 kV^{-1} applied to all carbon resistors.

filename	HV	rings up	down	method	calculated size
ceres31	-30.0 kV	b=0.26	b=0.345	Maxwell auto mesh	2x1/4 chamber
ceres54	-30.0 kV	b=0.27	b=0.36	Maxwell manual mesh	1/2 chamber
ceres86	-29.2 kV	b=0.24	b=0.34	mymax	1/2 chamber
ceres180	0 kV	$U_1(r)$	–	mymax	1/2 chamber
ceres181	0 kV	$U_2(r)$	–	mymax	1/2 chamber
ceres182	0 kV	$U_3(r)$	–	mymax	1/2 chamber
ceres190	0 kV	–	$U_1(r)$	mymax	1/2 chamber
ceres191	0 kV	–	$U_2(r)$	mymax	1/2 chamber
ceres192	0 kV	–	$U_3(r)$	mymax	1/2 chamber
ceres87	ceres86 combined with weighted 180-182 and 190-192				1/2 chamber

Table 5: Two dimensional potential maps for misalignment correction. The maps ceres200-219 are the two dimensional correction fields that need to be added to the three-dimensional map at planes 00-19, respectively, and were obtained as a linear combination of appropriately rotated maps ceres300-330.

filenames	HV	displacement	tilt	method	calculated size
ceres300-308	-30.0 kV	0	0..8 mr	mymax2d	16 chambers
ceres310-330	-30.0 kV	-2..2 mm	0	mymax2d	16 chambers
ceres320	-30.0 kV	0	0	mymax2d	16 chambers
ceres200-219	0.0 kV	fit	fit	lin. comb.	16 chambers

11 Determination of the electron mobility and the electronics time offset

Ideally, the electric field should be known before one starts reconstructing tracks. In practice, however, as discussed in the previous section, reconstructed hits were heavily used in the determination of the field. This means that the drift velocity and the electric field had to be studied at the same time (or iteratively). The drift velocity calibration, which in this manner becomes part of the electric field determination procedure, is described in this section. (Some of) the constants relevant to the electron drift are collected in Table 6.

Since the drift velocity in first order scales with the electric field it is convenient to consider the ratio of the two, called mobility. The knowledge of the mobility for different

Table 6: Collection of numbers relevant for electron drift in the TPC.

clock frequency	3.4 MHz
1 timebin	0.29412 μs
maximum drift velocity	7.0 mm/timebin = 2.4 cm/μs
minimum drift velocity	2.6 mm/timebin = 0.9 cm/μs
typical drift calculation step here	0.5 μs

values of the electric field is essential for understanding drift in a radial field. Seven approximately parallel laser rays in the special sector of the TPC, together with the signal from the HV cylinder, were used to determine the electron mobility function. This was achieved by minimizing radial distances of the reconstructed TPC hits from the expected track positions (Fig. 20). The expected track positions were calculated from the laser beam position before entering the TPC, measured with the position sensitive diodes, and the known mirror positions and angles. The track at r=1100 mm,

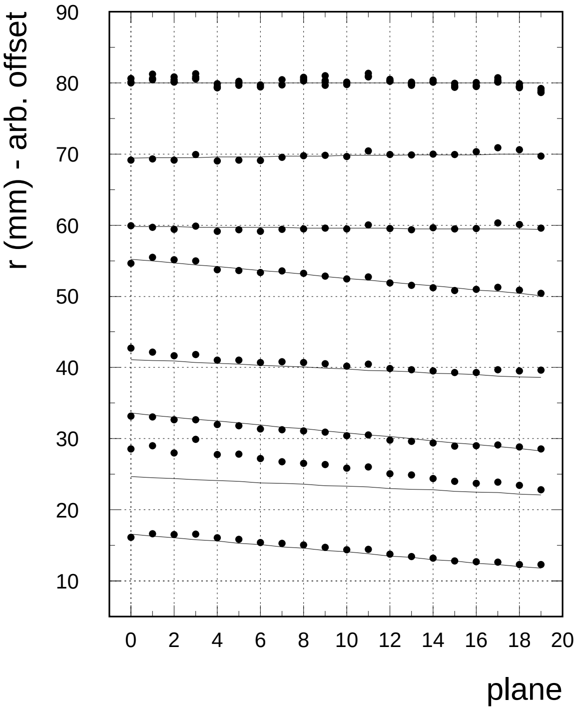

Figure 20: Reconstructed laser tracks and the HV cylinder after the 12-parameter field/mobility fit. The points and the lines represent calibrated TPC measurements and the expected track positions based on the diode information, respectively. The vertical scale has been adjusted by adding arbitrary offsets to the tracks in order to bring them closer to each other. The uppermost set of points represents the cylinder, then come the laser tracks at r = 600, 700, 800, 900, 1000, 1100, and 1200 mm.

for which the mirror angle seems to deviate systematically from the assumed value, was excluded from the fit. In the case of the cylinder signal the reconstructed radius was compared to the nominal 486 mm. The 12 fit parameters included three factors for electric field corrections at each TPC end (see Section 6), five parameters of the electron mobility curve, and the time offset.

The five-parameter mobility curve obtained from the fit is shown as the solid line in Fig. 21. The five parameters are the mobility values at E = 10, 25, 35, 45, and 65 V/mm, the rest of the curve being an interpolation [5] between these points. This trick couples the parameters to specific drift regions and thus helps the fit to converge quickly. The obtained mobility is compared to a calculation performed with the drift simulation package Garfield/Magboltz [6], represented in Fig. 21 by the solid line. The deviation is significant and cannot be removed by small changes in the input gas composition or temperature (dashed and dash-dotted lines).

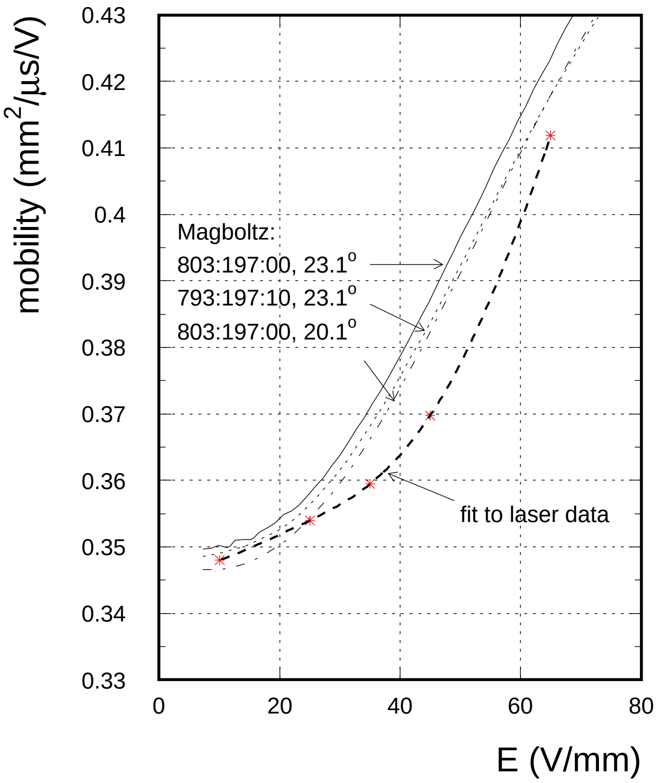

Figure 21: Mobility (ratio of drift velocity and electric field) obtained from the fit to the laser data (dashed line with stars). For comparison, the solid, the dotted, and the dash-dotted lines show the mobility as calculated with Magboltz[6] for three gas composition (Ne:CO_2:N_2) and temperature cases.

12 Drift field calibration strategy summarized

Altogether the following parameters have been determined in the course of calibration:

- Drift voltage, i.e. potential of the high voltage cylinder
- "Badness" of the resistors, i.e the resistance drop under load
- Five parameters of the mobility vs. electric field curve
- Three amplitudes of the smile correction fields at the upstream end of TPC
- Three amplitudes of the smile correction fields at the downstream end of TPC
- 20x16=320 chamber displacements
- 20x16=320 chamber tilts
- Global electronics time offset
- 3x16x20=960 FEB time offsets
- tribump: two coefficients parametrizing the 48 individual pad time offsets across the chamber

The operational order of calibration was, roughly, as follows:

1. Assume some value of the drift voltage (i.e. potential of the high voltage cylinder).
2. Calculate the actual potential at the gating grid (Section 2).
3. Use central part (planes 5-14) of the 7 laser tracks to determine 4 of the 5 mobility parameters and the global time offset (Section 11).
4. Use upstream part (planes 0-4) of the 7 laser tracks to determine the upstream correction fields coefficients (Section 7).
5. Use downstream part (planes 15-19) of the 7 laser tracks to determine the downstream correction fields coefficients (Section 7).
6. Use edge position in the radial hit distribution to determine the displacements and tilts of the chambers, FEB time offsets, tribump, and the last parameter of the mobility, responsible for the mobility at the lowest field (Section 8).

Since the drift depends on the field, and the field determination procedure depends on the drift, some iterations were necessary.

References

[1] http://esumi.home.cern.ch/esumi/Welcome77.html

[2] Hannes, private communication

[3] Bernd Windelband's collection of drawings

[4] http://wwwinfo.cern.ch/ce/ae/Maxwell/Maxwell.html

[5] `DIVDIF` (CERNLIB)

[6] R. Veenhof, Nucl. Instr. and Meth. A 419 (2-3) (1998) 726; S.F. Biagi, Nucl. Instr. and Meth. A 421 (1-2) (1999) 234.